(Received 7 January 2026, Accepted 28 January 2026, Scheduled 23 February 2026)

# Optimizing Sensorless Control in PMSM Based on the TOGIFO-X Flux Observer Algorithm

Jianwei Liang, Shuxin Pan*, Jie Yue, Jiaming Tian, and Jingxuan Sun

*School of Electrical Engineering and Automation*
*Jiangxi University of Science and Technology, Ganzhou 341000, Jiangxi, China*

**ABSTRACT:** Flux observers have been extensively employed in the sensorless control of permanent magnet synchronous motors (PMSMs). Traditional flux observers are susceptible to DC offset and high-order harmonics during flux estimation. To address this issue, this paper proposes an improved third-order generalized integrator (TOGIFO-X), which combines a third-order generalized integrator with a low-pass filter. First, the relationship between the flux observation error and rotor position error is established. Then, through rigorous mathematical derivation and Bode-plot analysis, the proposed TOGIFO-X was compared with three conventional flux observers, demonstrating its capability to effectively eliminate both the DC component and high-order harmonic components in the estimated rotor flux without introducing any adverse effects on the amplitude or phase of the fundamental wave. Finally, the effectiveness of the improved third-order generalized integrator is verified via simulations and a 0.75 kW surface-mounted PMSM (SPMSM) experimental platform. The experimental results indicate that TOGIFO-X significantly enhances the reduction in flux estimation error and the elimination of DC bias, thereby contributing to improved position estimation accuracy and advances in sensorless control technology.

## 1. INTRODUCTION

Permanent magnet synchronous motors (PMSMs) are widely used in various fields, such as household appliances, medical equipment, and transportation owing to their advantages of high torque density, long lifespan, wide speed regulation range, and high power factor [1]. Field-oriented control, also known as vector control, is the primary control method for PMSMs. This method requires accurate rotor position and speed information. However, traditional Hall sensors or encoders have shortcomings in signal reliability, environmental adaptability, installation, maintenance, and cost. These shortcomings reduce the robustness and competitiveness of drive systems [2]. Consequently, sensorless control strategies for PMSMs have become a research hotspot over the past few decades.

Currently, sensorless control strategies for PMSMs can be categorized into two main types [3]: high-frequency signal-injection methods [4] and fundamental wave estimation methods [5]. The former is mainly applied in zero and low-speed regions. However, the injected high-frequency signals bring additional harmonic power losses, torque/speed pulsations, and noise. The latter, also known as the back-electromotive force (back-EMF) method, is mainly employed in medium to high-speed regions and is widely utilized in the design of various observers, such as sliding mode observers (SMO) [6], extended Kalman filters (EKF) [7], Luenberger observers [8], and flux observers [9]. Flux observers have been extensively studied in recent years owing to their simplicity and ease of implementation.

Flux observers can be divided into current and voltage models, with the voltage model being the most commonly used [10]. Traditional flux observers typically employ a pure integrator to obtain the rotor position information. However, pure integration suffers from issues such as initial value uncertainty and integral drift, which lead to distortion in the rotor position waveform. To address this problem, Feng et al. [11] proposed using a low-pass filter (LPF) instead of a pure integrator for flux observations. While the DC offset decays exponentially over time when using an LPF, it introduces a phase delay and amplitude attenuation, necessitating corresponding compensation. Furthermore, severe waveform distortion occurs when the operating frequency of the motor falls below the cutoff frequency of the LPF.

The second-order generalized integrator (SOGI) is well known for its excellent filtering, quadrature signal generation, and phase extraction capabilities. It is highly effective in achieving a 90° phase shift for grid voltage signals and effectively filters high-order harmonics, leading to its widespread use in grid applications. Jiang et al. [12] proposed a second-order generalized integrator flux observer (SOGIFO) capable of achieving a sensorless control system based on rotor flux estimation over a wide speed range; however, its ability to eliminate the DC offset is limited. Zhao et al. [13] developed a multi-SOGI-FLL flux observer for induction motors that can accurately estimate the rotor flux while effectively reducing the DC offset and high-order harmonics; however, some deficiencies in DC offset elimination remain. Jiang et al. [14] proposed a third-order generalized integrator flux observer (TOGIFO) that can effectively eliminate the DC component but has limited suppression of high-order harmonics. Xu et

* Corresponding author: Shuxin Pan (2655018491@qq.com).

al. [15] introduced a fourth-order generalized integrator flux observer, which performs excellently in eliminating the DC offset and harmonics but significantly increases the computational burden.

To address the aforementioned issues, this study combines a third-order generalized integrator with a low-pass filter and proposes an improved third-order generalized integrator-based flux observer (Extended, TOGIFO-X). Utilizing a third-order transfer function, theoretical analysis verified its strong attenuation capability for DC offset and harmonics, thereby significantly improving the flux estimation accuracy and rotor position determination. Its advantages include a wide speed range, simple implementation, and the ability to eliminate DC offsets and harmonics. Consequently, no additional parameter identification or disturbance attenuation structures are required. Notably, this method can be employed within a 3% to 100% rated speed range, whereas most back-EMF estimation-based sensorless control strategies are ineffective below 5% rated speed. Finally, experiments were conducted on the experimental platform. The results demonstrate that TOGIFO-X outperforms the three conventional flux observers in terms of steady-state performance, dynamic performance, and DC disturbance rejection capability, which verifies the effectiveness of the proposed method.

The remainder of this paper is organized as follows. Section 1 introduces a sensorless control algorithm for PMSMs based on the rotor flux observer and briefly analyzes the pure integrator, LPF, and SOGI-based rotor flux observers. TOGIFO-X and its analysis are presented in Section 2. The simulated and experimental results are presented in Sections 3 and 4, respectively. Finally, conclusions are presented in Section 5.

## 2. PMSM SENSORLESS CONTROL BASED ON ROTOR FLUX OBSERVER

### 2.1. Fundamental Principle of the Flux Observer

To simplify the derivation, non-ideal factors such as core saturation, eddy current, and hysteresis losses are neglected. The voltage and flux equations for a surface-mounted permanent magnet synchronous motor (SPMSM) in a stationary coordinate system are expressed as:

$$\begin{bmatrix} u_\alpha \\ u_\beta \end{bmatrix} = \begin{bmatrix} R_s & 0 \\ 0 & R_s \end{bmatrix} \begin{bmatrix} i_\alpha \\ i_\beta \end{bmatrix} + p \begin{bmatrix} \Psi_\alpha \\ \Psi_\beta \end{bmatrix} \tag{1}$$

$$\begin{bmatrix} \Psi_\alpha \\ \Psi_\beta \end{bmatrix} = L \cdot \begin{bmatrix} i_\alpha \\ i_\beta \end{bmatrix} + \psi_f \cdot \begin{bmatrix} \cos(\theta_e) \\ \sin(\theta_e) \end{bmatrix} \tag{2}$$

where $u_s = \begin{bmatrix} u_\alpha & u_\beta \end{bmatrix}^T$ is the stator voltage vector; $R_s$ is the stator resistance; $i_s = \begin{bmatrix} i_\alpha & i_\beta \end{bmatrix}^T$ is the stator current vector; $p$ is the derivative; $\Psi_s = \begin{bmatrix} \Psi_\alpha & \Psi_\beta \end{bmatrix}^T$ is the stator flux linkage vector; $L$ is the stator inductance; $\psi_f$ is the permanent magnet flux linkage; and $\theta_e$ is the actual rotor electrical position.

The back-EMF can be obtained by differentiating the flux linkage:

$$\begin{bmatrix} e_\alpha \\ e_\beta \end{bmatrix} = p \cdot \psi_f \cdot \begin{bmatrix} \cos(\theta_e) \\ \sin(\theta_e) \end{bmatrix} = \begin{bmatrix} -\omega_e \psi_f \sin(\theta_e) \\ \omega_e \psi_f \cos(\theta_e) \end{bmatrix} \tag{3}$$

where $e_r = \begin{bmatrix} e_\alpha & e_\beta \end{bmatrix}^T$ is the back-EMF vector, and $\omega_e$ is the rotor electrical angular velocity. State variables $x$ and $y$ were constructed accordingly. Here, $x = \begin{bmatrix} x_\alpha & x_\beta \end{bmatrix}^T$ is the stator flux linkage vector $\Psi_s$, and $x - Li_s$ is the rotor flux linkage vector $\Psi_r = \begin{bmatrix} \Psi_{r\alpha} & \Psi_{r\beta} \end{bmatrix}^T$, $y = \begin{bmatrix} y_\alpha & y_\beta \end{bmatrix}^T$ is the back electromotive force vector.

$$\begin{bmatrix} x_\alpha \\ x_\beta \end{bmatrix} = L \cdot \begin{bmatrix} i_\alpha \\ i_\beta \end{bmatrix} + \psi_f \cdot \begin{bmatrix} \cos(\theta_e) \\ \sin(\theta_e) \end{bmatrix} \tag{4}$$

$$\begin{bmatrix} y_\alpha \\ y_\beta \end{bmatrix} = \begin{bmatrix} u_\alpha \\ u_\beta \end{bmatrix} - \begin{bmatrix} R_s & 0 \\ 0 & R_s \end{bmatrix} \begin{bmatrix} i_\alpha \\ i_\beta \end{bmatrix} \tag{5}$$

Based on Equations (1), (2), and (3), a state-space equation can be formulated as

$$\dot{x} = y \tag{6}$$

To establish a nonlinear observer, the stator flux linkage is defined as the vector function $\eta(x)$

$$\eta(x) = x - L \begin{bmatrix} i_\alpha \\ i_\beta \end{bmatrix} \tag{7}$$

According to Equation (7), its two-norm is $\|\eta(x)\|^2 = \psi_f^2$. The final expression for a nonlinear flux observer is as follows:

$$\dot{\hat{x}} = y + \frac{\gamma}{2}\eta(\hat{x}) \left[\psi_f^2 - \|\eta(\hat{x})\|^2\right] \tag{8}$$

where $\hat{x}$ is the observer state variable, $\dot{\hat{x}}$ its derivative, $\gamma$ the observer gain coefficient, and $\gamma > 0$.

The rotor electrical angle is calculated from the state variable obtained $\hat{x}$ by the observer, which contains the rotor position information

$$\hat{\theta}_e = \tan^{-1}\left(\frac{\hat{x}_\beta - Li_\beta}{\hat{x}_\alpha - Li_\alpha}\right) = \tan^{-1}\left(\frac{\hat{\Psi}_{r\beta}}{\hat{\Psi}_{r\alpha}}\right) \tag{9}$$

where $\hat{\theta}_e$ denotes the estimated electrical angle. After obtaining $\hat{\theta}_e$, the estimated rotor angular velocity $\hat{\omega}_e$ can be derived using a differentiator or phase-locked loop (PLL). Equation (9) shows that the accuracy of the rotor flux linkage vector estimation directly affects that of the final rotor position estimation.

A traditional observer comprises a pure integrator. From Equation (3), the rotor flux linkage can be obtained by integrating the back-EMF

$$\Psi_r = \int (u_s - R_s i_s - L_p \dot{i}_s) dt = \int e_r dt \tag{10}$$

During motor operation, stator inductance and resistance are affected by temperature. Other issues include parameter mismatch, inverter nonlinearities, uncertain integration initial values, detection errors, and noise [16], and the back-EMF vector can be expressed as:

$$e_r = u_s - (R_{s0} + \Delta R_s)\, i_s - (L_0 + \Delta L)\, p i_s + e_{r0} + \chi \quad (11)$$

where $R_{s0}$ is the nominal stator resistance; $\Delta R_s$ is its variation; $L_0$ is the nominal stator inductance; $\Delta L$ is its variation; $\Psi_{r0} = \begin{bmatrix} \Psi_{r\alpha}(0) & \Psi_{r\beta}\ (0) \end{bmatrix}^T$ is the nominal permanent magnet flux linkage; $e_{r0} = p\Psi_{r0}$ is the compensation factor. In the form of DC, fundamental, and harmonic components, Equation (11) can be rewritten as

$$e_r = A_0 + A_1 \sin(\omega_1 t + \varphi_1) + \sum_{n=2}^{\infty} A_n \sin(\omega_n t + \varphi_n) \quad (12)$$

where $A_0 = \begin{bmatrix} A_{\alpha 0} & A_{\beta 0} \end{bmatrix}$ is the DC component; $A_1 \sin(\omega_1 t + \varphi_1)$ is the fundamental component with amplitude $A_1 = \begin{bmatrix} A_{\alpha 1} & A_{\beta 1} \end{bmatrix}$; $\sum_{n=2}^{\infty} A_n \sin(\omega_n t + \varphi_n)$ is the sum of high-order harmonic components with amplitudes $A_n = \begin{bmatrix} A_{\alpha n} & A_{\beta n} \end{bmatrix}$; $\omega_1$ and $\omega_n$ are the fundamental and harmonic angular frequencies, respectively; $\varphi_1$ and $\varphi_n$ are the initial phases. Performing the Laplace transform on (12):

$$E_r(s) = \frac{A_0}{s} + A_1 \frac{s \sin\varphi_1 + \omega_1 \cos\varphi_1}{s^2 + \omega_1^2} + \sum_{n=2}^{\infty} A_n \frac{s \sin\varphi_n + \omega_n \cos\varphi_n}{s^2 + \omega_n^2} \quad (13)$$

where $E_r(s)$ is the Laplace transform of $E_r$, and $s$ is the Laplace operator.

### 2.2. Flux Observer Based on Pure Integrator

The traditional flux observer employs a pure integrator, represented by $\frac{1}{s}$ in the flux estimation process. Considering the aforementioned nonlinear disturbance factors, the observed rotor flux $E_r(s) \cdot \frac{1}{s}$, after the inverse Laplace transform, is expressed as

$$\Psi_{r\_I}(t) = A_0 t + \frac{A_1}{\omega_1}\cos(\varphi_1) + \sum_{n=2}^{\infty} \frac{A_n}{\omega_n}\cos(\varphi_n) + \frac{A_1}{\omega_1}\sin(\omega_1 t + \varphi_1 - 0.5\pi) + \sum_{n=2}^{\infty} \frac{A_n}{\omega_n}\sin(\omega_n t + \varphi_n - 0.5\pi) \quad (14)$$

where $A_0 t + \frac{A_1}{\omega_1}\cos(\varphi_1) + \sum_{n=2}^{\infty} \frac{A_n}{\omega_n}\cos(\varphi_n)$ is the DC offset component; $\frac{A_1}{\omega_1}\sin(\omega_1 t + \varphi_1 - 0.5\pi)$ is the fundamental component; and $\sum_{n=2}^{\infty} \frac{A_n}{\omega_n}\sin(\omega_n t + \varphi_n - 0.5\pi)$ is the higher-order harmonic component. The term $A_0 t$ indicates that the DC offset increases linearly with time, causing a significant drift in the integrator's output. This can severely affect the integration result, potentially lead to flux saturation, and consequently impaire rotor position estimation, jeopardizing the feasibility of sensorless control. Harmonic components may also adversely affect the position estimation.

### 2.3. Flux Observer Based on LPF

The LPF in the flux estimation is represented by $\frac{1}{s+\omega_c}$, where $\omega_c$ is the cutoff frequency. The rotor flux $E_r(s) \cdot \frac{1}{s+\omega_c}$, observed by the LPF-based flux observer after the inverse Laplace transform, is expressed as

$$\Psi_{r\_LPF}(t) = \frac{A_0}{\omega_c} - \frac{A_0 e^{-\omega_c t}}{\omega_c} + \frac{A_1 \cos(\varphi_1 + \theta_1) e^{-\omega_c t}}{\sqrt{\omega_1^2 + \omega_c^2}} + \sum_{n=2}^{\infty} \frac{A_n \cos(\varphi_n + \theta_n)}{\sqrt{\omega_n^2 + \omega_c^2}} + \frac{A_1}{\sqrt{\omega_1^2 + \omega_c^2}} \sin(\omega_1 t + \varphi_1 - 0.5\pi + \theta_1) + \sum_{n=2}^{\infty} \frac{A_n}{\sqrt{\omega_n^2 + \omega_c^2}} \sin(\omega_n t + \varphi_n - 0.5\pi + \theta_n) \quad (15)$$

where $\frac{A_0}{\omega_c} - \frac{A_0 e^{-\omega_c t}}{\omega_c} + \frac{A_1 \cos(\varphi_1+\theta_1) e^{-\omega_c t}}{\sqrt{\omega_1^2+\omega_c^2}} + \sum_{n=2}^{\infty} \frac{A_n \cos(\varphi_n+\theta_n)}{\sqrt{\omega_n^2+\omega_c^2}}$ is the DC offset component; $\frac{A_1}{\sqrt{\omega_1^2+\omega_c^2}} \sin(\omega_1 t+\varphi_1-0.5\pi+\theta_1)$ is the fundamental component; and the high-order harmonic component is $\sum_{n=2}^{\infty} \frac{A_n}{\sqrt{\omega_n^2+\omega_c^2}} \sin(\omega_n t+\varphi_n-0.5\pi+\theta_n)$. Equation (15) shows that the DC component decays exponentially with time. Although not completely eliminated, it effectively addresses the flux saturation issue. The amplitude of high-order harmonics is also reduced compared to that of the pure integrator. However, it is also evident from Equation (15) that the amplitude of the fundamental component is attenuated by a factor of $\frac{\omega_1}{\sqrt{\omega_1^2+\omega_c^2}}$, and its phase is delayed by $\theta_1 = \arctan\left(\frac{\omega_c}{\omega_1}\right)$ compared with the pure integrator. Therefore, using an LPF requires corresponding amplitude and phase compensation strategies.

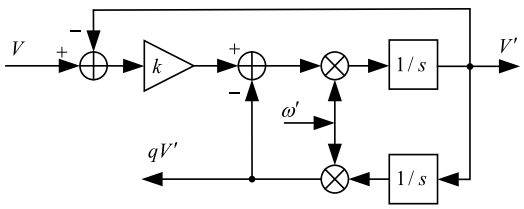


**FIGURE 1**. Block diagram of the SOGI structure.

### 2.4. Flux Observer Based on SOGI

The SOGI generates two orthogonal signals. Its structure is shown in Figure 1. The SOGI transfer functions are as follows:

$$D(s) = \frac{V'(s)}{V(s)} = \frac{k\hat{\omega}s}{s^2 + k\hat{\omega}s + \hat{\omega}^2} \tag{16}$$

$$Q(s) = \frac{qV'(s)}{V(s)} = \frac{k\hat{\omega}^2}{s^2 + k\hat{\omega}s + \hat{\omega}^2} \tag{17}$$

where $V$ is the sinusoidal input signal, $k$ the damping coefficient, and $\hat{\omega}$ the estimated angular velocity of the observer.

When the observer's estimated angular velocity $\hat{\omega}$ matches the frequency of the input signal $V$, the phase of the output signal $V'$ aligns with $V$, and $V'$ and $qV'$ become sinusoidal waves with equal amplitudes and a 90° phase difference. $D(s)$ and $Q(s)$ are typically used for filtering and integration, respectively. In the steady state, defining $s = j\hat{\omega}$, $qV'$ can be viewed as the integral of the input signal and calculated as

$$Q(s) = \frac{k\hat{\omega}^2}{-\hat{\omega}^2 + k\hat{\omega}s + \hat{\omega}^2} = \frac{1}{s}\hat{\omega} \tag{18}$$

From Eq. (18), $Q(s)$ can be regarded as an integrator. The second-order generalized integrator flux observer (SOGIFO) uses the back-EMF signal as the input to the SOGI, obtains its quadrature outputs, and extracts the estimated rotor angular velocity $\hat{\omega}$ via a PLL or arctangent function. The structure of the SOGIFO is shown in Figure 2.

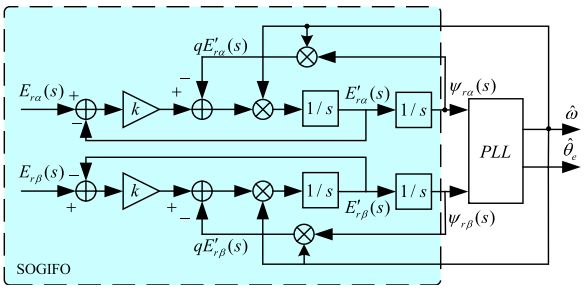


**FIGURE 2**. Block diagram of the SOGIFO structure.

The rotor flux $E_r(s) \cdot Q(s) \cdot \frac{1}{\hat{\omega}}$ observed by SOGIFO after the inverse Laplace transform is expressed as

$$\Psi_{r\_SOGIFO}(t) = \frac{A_0 k}{\omega_1} + \frac{A_1}{\omega_1}\sin(\omega_1 t + \varphi_1 - 0.5\pi) + \sum_{n=2}^{\infty}\frac{A_n}{\omega_n}\cdot\frac{1}{\sqrt{\frac{(1-n^2)^2}{k^2n^4}+1}} \cdot \sin(\omega_n t + \varphi_n - 0.5\pi + \gamma_{n1}) \tag{19}$$

where $\frac{A_0 k}{\omega_1}$ is the DC component; $\frac{A_1}{\omega_1}\sin(\omega_1 t+\varphi_1-0.5\pi)$ is the fundamental component; and $\sum_{n=2}^{\infty}\frac{A_n}{\omega_n}\cdot\frac{1}{\sqrt{\frac{(1-n^2)^2}{k^2n^4}+1}}\cdot\sin(\omega_n t+\varphi_n-0.5\pi+\gamma_{n1})$ is the high-order harmonic component. Compared with the pure integrator, the DC component does not grow over time, the fundamental component exhibits no amplitude attenuation or phase shift, and the amplitude of the high-order harmonics is significantly attenuated. However, the DC offset was not eliminated.

## 3. FLUX OBSERVER BASED ON TOGIFO-X

To overcome the limitations of traditional flux observers, this study proposes a TOGIFO-X flux observer for PMSM rotor flux observation. This method combines a third-order generalized integrator with a low-pass filter to form an extended third-order generalized integrator (TOGI-X). It can effectively eliminate DC offset and high-order harmonics during rotor flux observation. Figure 3 shows the block diagram of the TOGI-X structure.

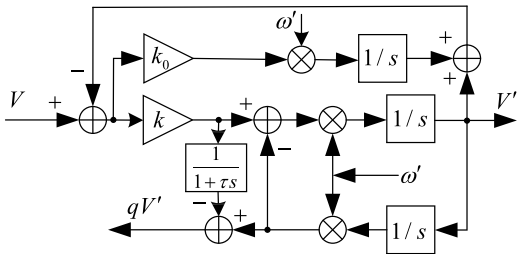


**FIGURE 3**. Block diagram of the TOGI-X structure.

The corresponding transfer functions for TOGI-X are:

$$D(s) = \frac{V'}{V} = \frac{k\hat{\omega}s^2}{s^3 + (k+k_0)\hat{\omega}s^2 + \hat{\omega}^2 s + k_0\hat{\omega}^3} \tag{20}$$

$$Q(s) = \frac{qV'}{V} = \frac{ks(\hat{\omega}^2\tau s - s^2)}{[s^3 + (k+k_0)\hat{\omega}s^2 + \hat{\omega}^2 s + k_0\hat{\omega}^3](1+\tau s)} \tag{21}$$

where $k$ and $k_0$ are damping coefficients, and $\tau$ is the time constant of the low-pass filter. Similar to SOGI, $D(s)$ is used for filtering, and $Q(s)$ is used for integration. $qV'$ can be regarded as the integrated flux of the input back-EMF signal. In the steady state, defining $s = j\hat{\omega}$, it is defined as:

$$Q(s) = \frac{ks\left(\hat{\omega}^2\tau s + \hat{\omega}^2\right)}{(1+\tau s)\left[s^3 - (k+k_0)\hat{\omega}^3 + k\hat{\omega}^3 + k_0\hat{\omega}^3\right]} = \frac{1}{s}\hat{\omega} \tag{22}$$

From Equation (22), $Q(s)$ in the TOGI-X can also be viewed as an integrator. The final structure of the TOGIFO-X is shown in Figure 4. The rotor flux observed by the TOGIFO-X observer is

$$\Psi_{r\_TOGIFO\text{-}X}(s) = \frac{1}{\hat{\omega}}\cdot Q(s)\cdot E_r(s) = \frac{1}{\hat{\omega}}\cdot\frac{ks(\hat{\omega}^2\tau s + \hat{\omega}^2)}{(1+\tau s)\left[s^3 - (k+k_0)\hat{\omega}^3 + k\hat{\omega}^3 + k_0\hat{\omega}^3\right]}\cdot E_r(s) \tag{23}$$

Combining Equations (13) and (23) and performing an inverse Laplace transform on Equation (23), we obtain:

For the DC component:

$$s\Psi_{r\_TOGIFO\text{-}X}(s) = s\frac{A_0}{s}\frac{1}{\hat{\omega}} \quad \frac{ks(\hat{\omega}^2\tau s - s^2)}{[s^3 + (k+k_0)\hat{\omega}s^2 + \hat{\omega}^2 s + k_0\hat{\omega}^3](1+\tau s)} \tag{24}$$

From Equation (24), when $k = 1.414$, the poles are located in the left half of the complex frequency plane, indicating the system stability. Applying the final value theorem,

$$\lim_{t\to\infty} \Psi_{r\_TOGIFO\text{-}X}(t) = \lim_{s\to 0} s\Psi_{r\_TOGIFO\text{-}X}(s)$$

$$= \lim_{s\to 0} s\frac{A_0}{s}\frac{1}{\hat{\omega}}\frac{ks\left(\hat{\omega}^2\tau s - s^2\right)}{\left[s^3 + (k+k_0)\hat{\omega}s^2 + \hat{\omega}^2 s + k_0\hat{\omega}^3\right](1+\tau s)} \quad (25)$$

For the fundamental component, Substituting $s = j\hat{\omega}$ into Equation (23) yields:

$$\Psi_{r\_TOGIFO\text{-}X}(t)$$

$$= \frac{1}{\hat{\omega}}\frac{ks(\hat{\omega}^2\tau s - s^2)}{\left[s^3 + (k+k_0)\hat{\omega}s^2 + \hat{\omega}^2 s + k_0\hat{\omega}^3\right](1+\tau s)}E_r(s)$$

$$= \frac{1}{\hat{\omega}}\cdot\frac{ks(\hat{\omega}^2\tau s + \hat{\omega}^2)}{\left[s^3 - (k+k_0)\hat{\omega}^3 + k\hat{\omega}^3 + k_0\hat{\omega}^3\right](1+\tau s)}\cdot e_r(t)$$

$$= \frac{1}{j\hat{\omega}}\cdot\sin(\omega_1 t + \varphi_1)\cdot e_r(t) = \frac{A_1}{\hat{\omega}}\sin(\omega_1 t + \varphi_1 - 0.5\pi) \quad (26)$$

For high-order harmonic components, let $\tau = \frac{2\pi}{\hat{\omega}}$, and substituting $s = j\omega_n = jn\hat{\omega}$ into Equation (23) yields:

$$\begin{aligned}\Psi_{r\_TOGIFO\text{-}X}(t) &= \frac{1}{\hat{\omega}}\frac{ks(\hat{\omega}^2\tau s - s^2)}{\left[s^3 + (k+k_0)\hat{\omega}s^2 + \hat{\omega}^2 s + k_0\hat{\omega}^3\right](1+\tau s)}e_r(t)\\ &= e_r(t)\cdot\frac{kn^2\sqrt{4\pi^2+n^2}}{\hat{\omega}\cdot\sqrt{\left[k_0-(k+k_0)n^2\right]^2 + n^2(1-n^2)^2}\cdot\sqrt{1+4\pi^2n^2}}\angle\theta\\ &= \sum_{n=2}^{\infty}\frac{A_n}{\omega_n}\cdot\frac{\sin(\omega_n t + \varphi_n - 0.5\pi + \theta)}{\sqrt{\frac{[k_0-(k+k_0)n^2]^2+n^2(1-n^2)^2}{4\pi^2k^2n^4+k^2n^6}}\cdot\sqrt{\frac{1+4\pi^2n^2}{4\pi^2k^2n^4+k^2n^6}}}\end{aligned} \quad (27)$$

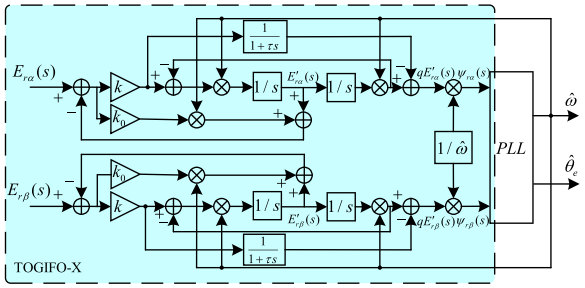


**FIGURE 4**. Block diagram of the TOGIFO-X structure.

where $\theta = \tan^{-1}(\frac{-n}{2\pi}) - \tan^{-1}(\frac{n-n^3}{k_0-kn^2-k_0n^2}) - \tan^{-1}(2\pi n)$. In summary, the steady-state rotor flux for TOGIFO-X can be expressed as:

$$\Psi_{r\_TOGIFO\text{-}X}(t) = \frac{A_1}{\hat{\omega}}\sin(\omega_1 t + \varphi_1 - 0.5\pi) + \sum_{n=2}^{\infty}\frac{A_n}{\omega_n}$$

$$\cdot\frac{\sin(\omega_n t + \varphi_n - 0.5\pi + \theta)}{\sqrt{\frac{[k_0-(k+k_0)n^2]^2+n^2(1-n^2)^2}{4\pi^2k^2n^4+k^2n^6}}\cdot\sqrt{\frac{1+4\pi^2n^2}{4\pi^2k^2n^4+k^2n^6}}} \quad (28)$$

Equation (28) shows three key results: first, the estimated DC component of the rotor flux is approximately 0; second, the fundamental component is consistent with that from the pure integrator; third, the amplitude of high-order harmonics is negatively correlated with the harmonic order, indicating effective harmonic attenuation. Furthermore, at the fundamental frequency, the added filter integration introduces no delay, enabling the precise filtering of interfering signals in the flux integration.

To further analyze the superiority of TOGIFO-X, Figure 5 shows the Bode plots of the four methods. Figure 5 illustrates

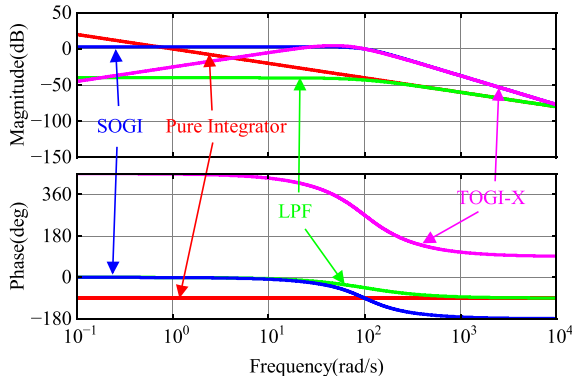


**FIGURE 5**. Bode plots.

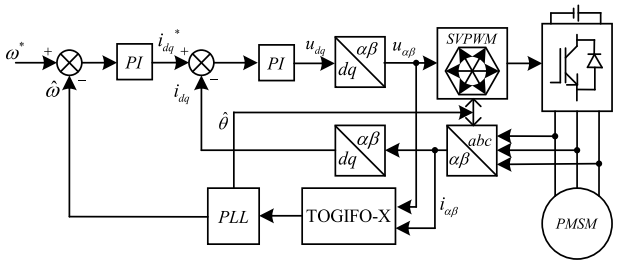


**FIGURE 6**. System simulation model.

the characteristics of the four methods. For the first-order integrator, DC offset increases over time and may cause integral saturation. The LPF can reduce DC offset and harmonics, but it also introduces phase shift and amplitude attenuation of the fundamental wave. SOGIFO achieves good attenuation of the DC offset and harmonic amplitudes without negatively affecting the fundamental waveform. However, its low-frequency magnitude response is 0 dB/decade, meaning that it cannot completely eliminate the DC offset. Finally, TOGIFO-X successfully eliminated DC offset and harmonic interference,

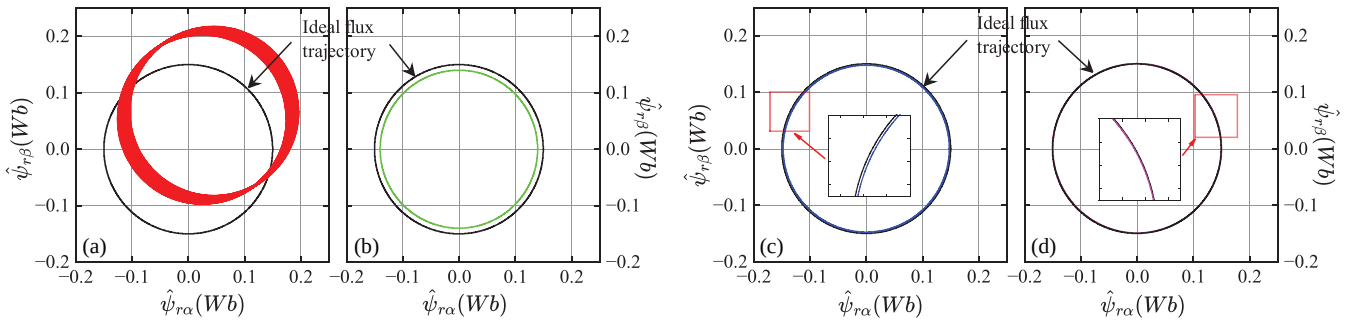


**FIGURE 7**. Estimated rotor flux loci at 1000 r/min. (a) Pure Integrator, (b) LPF, (c) SOGIFO, (d) TOGIFO-X.

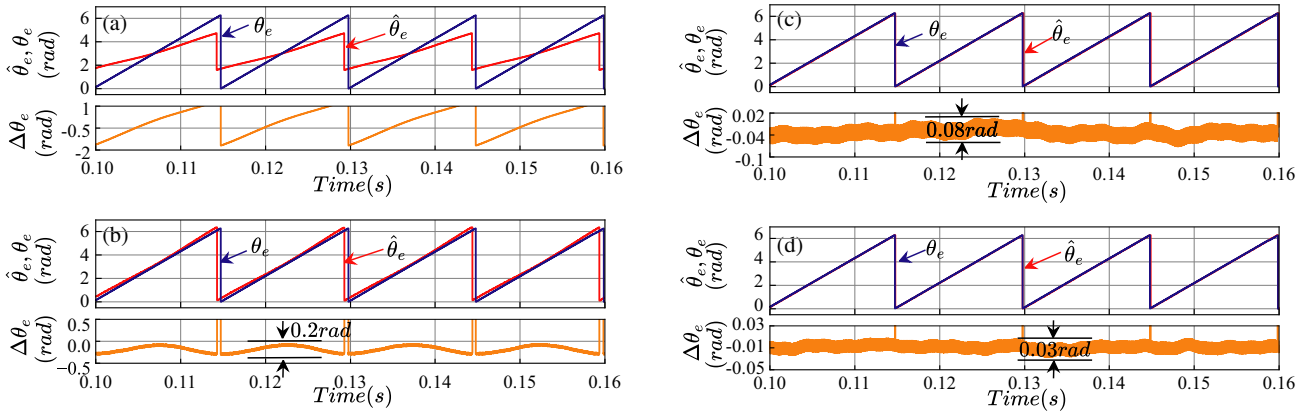


**FIGURE 8**. Estimated rotor position at 1000 r/min. (a) Pure integrator, (b) LPF, (c) SOGIFO, (d) TOGIFO-X.

with its magnitude frequency response attenuating at rates of −40 dB/decade at both low and high frequencies.

### 3.1. Simulation Verification

To validate the effectiveness of the proposed method, a PMSM drive system was designed based on MATLAB/Simulink, as shown in Figure 6.

The motor parameters used in the simulation and physical experiments are listed in Table 1.

**TABLE 1**. PMSM parameters.

| Symbol | Quantity | Value and Unit |
|---|---|---|
| $\Psi_f$ | Rotor Flux Linkage | 0.15 Wb |
| $P$ | Pole Pairs | 4 |
| $R_s$ | Stator Resistance | 2.88 Ω |
| $L_s$ | Stator Inductance | 6.4 mH |
| $P_n$ | Rated Power | 0.75 kW |
| $n_N$ | Rated Speed | 3000 r/min |

Figure 7 shows the estimated steady-state rotor flux loci and the ideal flux locus at no-load and 1000 r/min for the four methods. The ideal flux locus is represented by the black circle. The pure integrator generates large DC offset. As a result, its flux locus position drifts continuously and deviates from the ideal locus. The flux locus produced by the LPF exhibits amplitude attenuation compared with the ideal one. Both SOGIFO and TOGIFO-X tracked the ideal locus well, but the locus from TOGIFO-X was closer.

Figure 8 shows the estimated rotor position at a no-load 1000 r/min. The error for the pure integrator was significant. The LPF had an error of 0.2 rad and exhibits a phase shift. The SOGIFO error is 0.08 rad, and TOGIFO-X error is 0.03 rad. In summary, TOGIFO-X demonstrated the best position estimation capability among the four methods.

Figure 9 shows that the flux observation results on the $\alpha$-axis at a no-load 1000 r/min $\psi_\alpha$ is the actual $\alpha$-axis flux, and $\hat{\psi}_\alpha$ is the estimated $\alpha$-axis flux. The deviation of the flux from the $x$-axis indicates the presence of a DC component error, and the waveform curvature indicates high-order harmonics. As shown in Figure 9, the estimated flux from the pure integrator suffers severe amplitude attenuation with an error of 0.15 Wb. The flux estimated by the LPF showed an obvious DC offset causing a waveform shift, with an error of 0.1 Wb. Both SOGIFO and TOGIFO-X showed good flux estimation capability, with errors of 0.014 Wb and 0.004 Wb, respectively, close to zero. It indicates that TOGIFO-X had the best flux estimation performance.

Figure 10 shows the fast Fourier transform (FFT) analysis of the estimated flux from SOGIFO and TOGIFO-X at no-load 1000 r/min. The harmonics that significantly affect motor operation are mainly the 3rd, 5th, 7th, etc., with the 3rd, 5th, and 7th harmonics being predominant. As shown in Figure 10, the magnitudes of the 3rd, 5th, and 7th harmonics for TOGIFO-X were lower than those for SOGIFO.

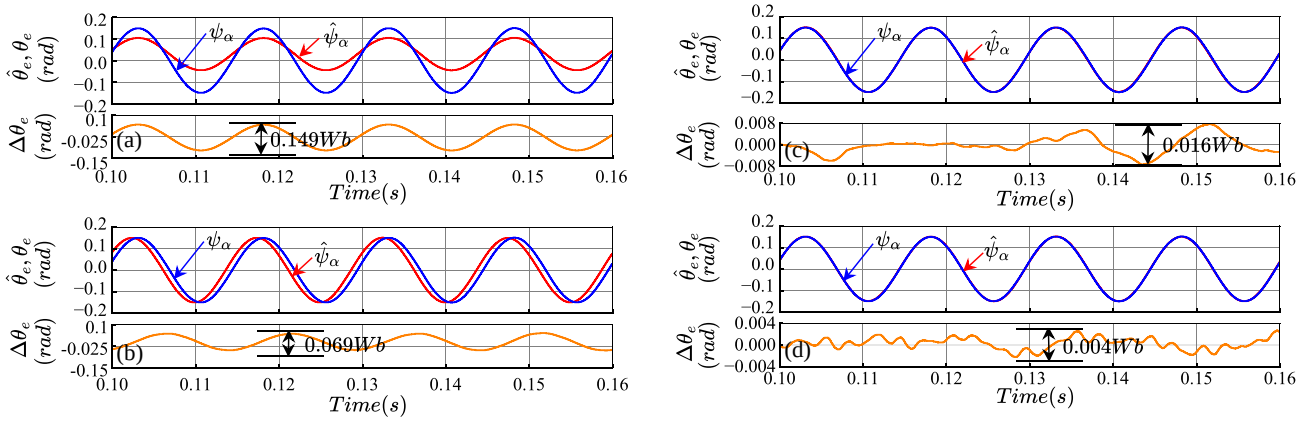


**FIGURE 9**. Estimated $\alpha$-axis flux at 1000 r/min. (a) Pure integrator, (b) LPF, (c) SOGIFO, (d) TOGIFO-X.

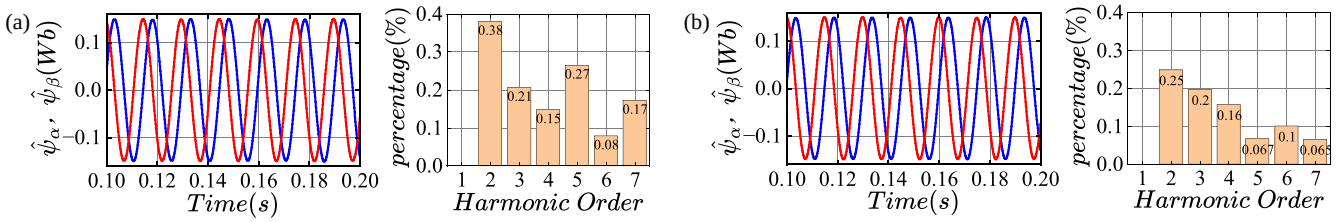


**FIGURE 10**. Estimated flux and FFT analysis at 1000 r/min (a) SOGIFO, (b) TOGIFO-X.

## 4. EXPERIMENTAL VERIFICATION

To further validate the effectiveness of the proposed method, a series of experiments was conducted on an SPMSM test platform, as shown in Figure 11. The main control board used was an STM32G474 microcontroller. The motor parameters are identical to those used in the simulations. The inverter switching frequency was 10 kHz, and the sampling period for the sensorless control algorithm was $1 \times 10^{-4}$ s. The following experiments primarily compared SOGIFO and TOGIFO-X. Because neither can start from zero speed or be used during startup, the SPMSM was initially started using I/F algorithm before switching to the sensorless algorithm in this study.

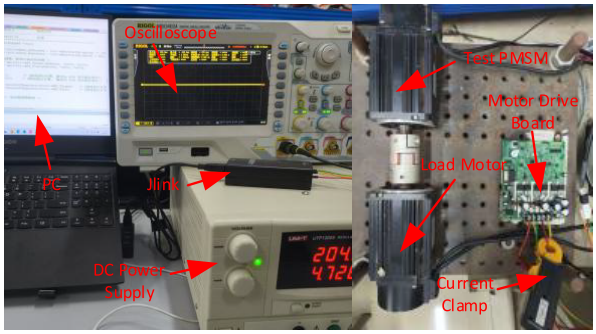


**FIGURE 11**. Experimental platform.

### 4.1. Steady-State Experiments

Figures 12(a) and (b) show the comparative experimental results for SOGIFO and TOGIFO-X under no-load at 100 r/min, respectively. The waveforms are arranged from top to bottom as follows: estimated speed, estimated flux, estimated position versus actual position, and position error. This order is consistent for dynamic and DC disturbance experiments. As shown in Figure 12(a), the maximum speed deviation for SOGIFO was 11 r/min. Simultaneously, owing to an estimated flux deviation of 0.001 Wb, the estimated position was inaccurate, with a maximum position estimation error of 0.521 rad. By contrast, in Figure 12(b), TOGIFO-X reduces the maximum speed error and position estimation error to 6 r/min and 0.126 rad, respectively. Owing to the low signal-to-noise ratio (SNR) at low speeds, the flux estimated by SOGIFO was severely distorted.

As shown in Figure 13, at 2000 r/min, the back-EMF SNR was sufficiently high. Compared to the low-speed range, the position estimation errors for the two methods decreased to 0.161 and 0.045 rad, respectively. The rotorposition estimation error decreased as the speed increased.

Based on the above analysis, compared to SOGIFO, TOGIFO-X exhibits a better rotor position estimation accuracy under low-speed steady-state conditions. As the speed increases, the estimation performance of both methods gradually converges, but TOGIFO-X maintains a superior speed and position estimation capability.

### 4.2. Dynamic Experiments

Figure 14 shows the experimental results under a step-rated load disturbance of 1000 r/min. A 5N load was suddenly applied at 1 s and removed at 1.5 s. As shown in Figure 14, when the load is suddenly applied, the maximum rotor position estimation error for TOGIFO-X is 0.532 rad, which is smaller than SOGIFO's value of 0.968 rad. The same applies during the load removal. Furthermore, the speed overshoot is significantly improved from 61 r/min to 31 r/min.

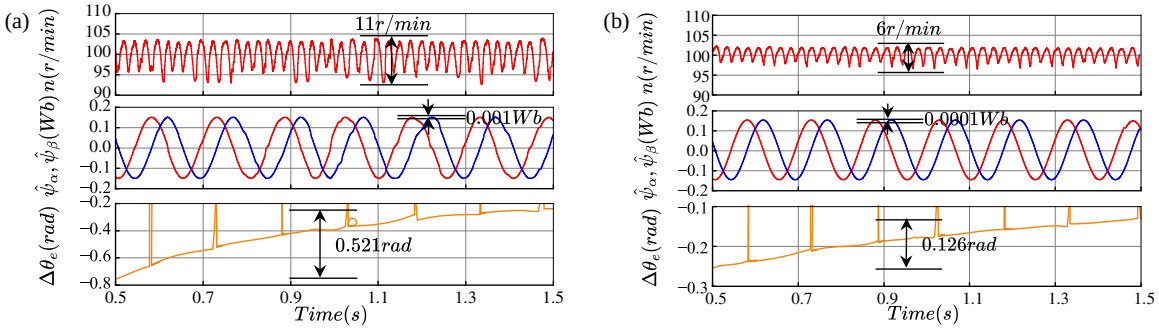


**FIGURE 12**. Estimated speed, flux and position error at 100 r/min. (a) SOGIFO, (b) TOGIFO-X.

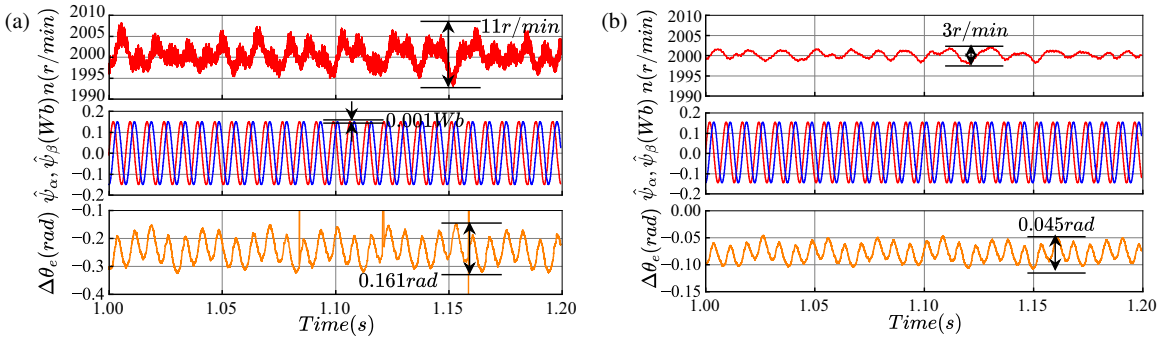


**FIGURE 13**. Estimated speed, flux, and position error at 2000 r/min. (a) SOGIFO, (b) TOGIFO-X.

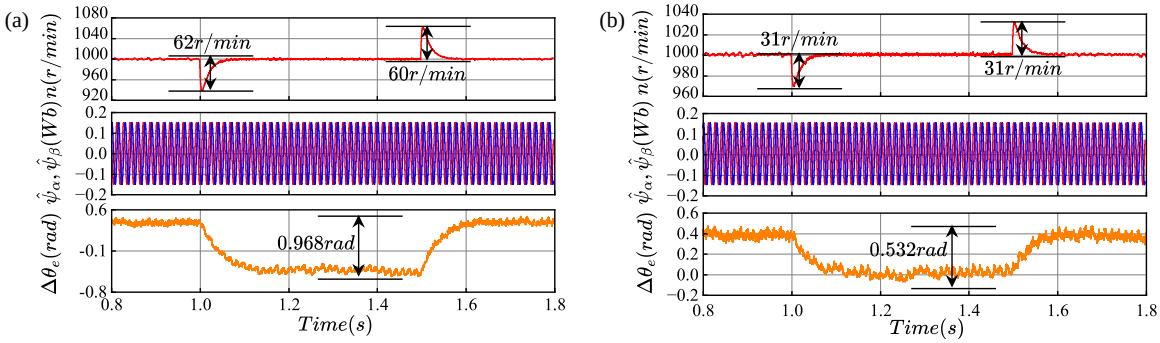


**FIGURE 14**. Estimated speed, flux and position error under step load disturbance at 1000 r/min. (a) SOGIFO, (b) TOGIFO-X.

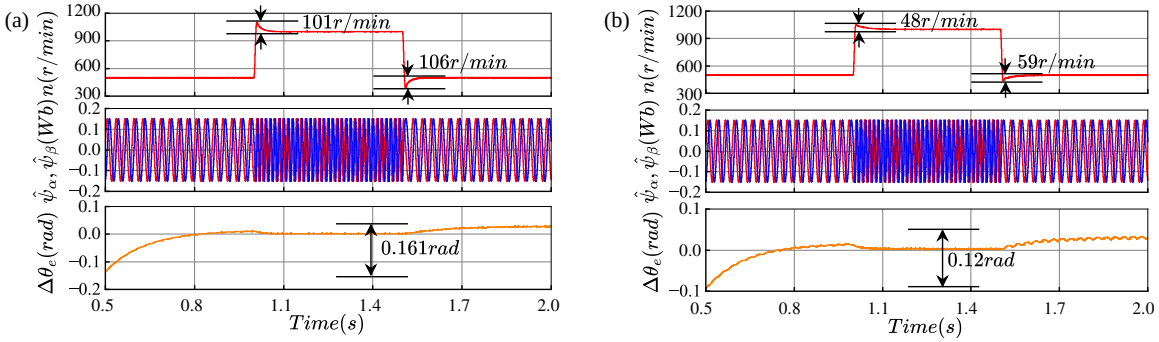


**FIGURE 15**. Estimated speed, flux and position error during speed transient. (a) SOGIFO, (b) TOGIFO-X.

To further validate the dynamic performance of the proposed method, Figure 15 shows the experimental results for a speed change from 500 to 1000 r/min. It can be observed that both methods estimate speed well, but TOGIFO-X exhibits a lower speed overshoot during both acceleration and deceleration than SOGIFO. The maximum position estimation error before and after the speed change was also reduced from 0.161 rad for SOGIFO to 0.12 rad for TOGIFO-X.

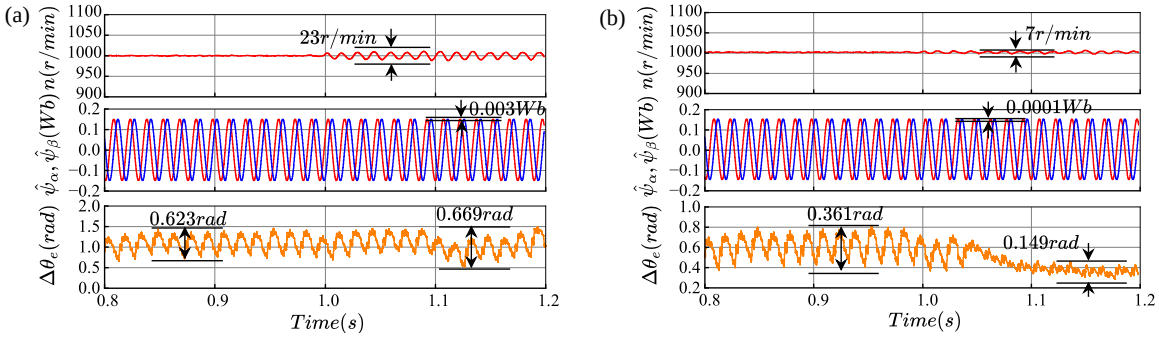


**FIGURE 16**. Estimated speed, flux, and position error under voltage disturbance. (a) SOGIFO, (b) TOGIFO-X.

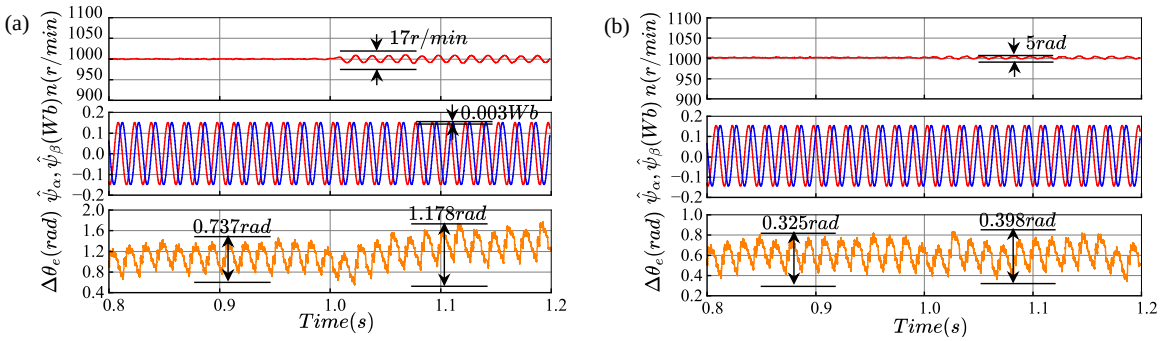


**FIGURE 17**. Estimated speed, flux, and position error under current disturbance. (a) SOGIFO, (b) TOGIFO-X.

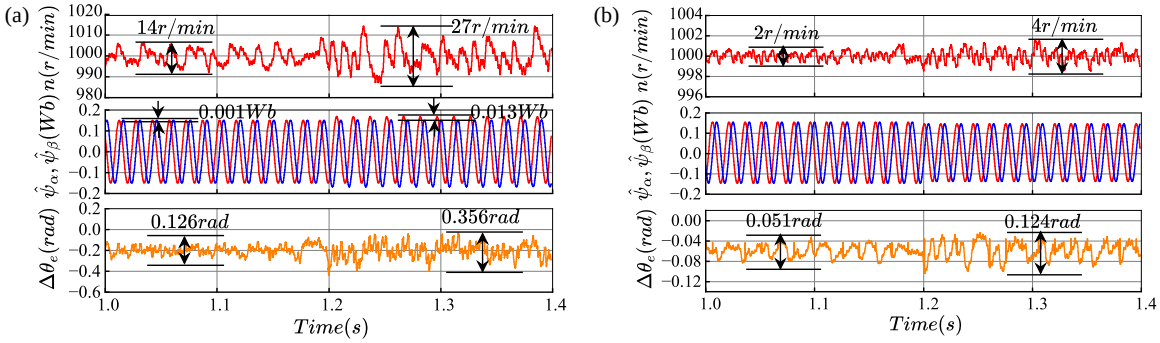


**FIGURE 18**. Estimated speed, flux, and position error under parameter mismatch. (a) SOGIFO, (b) TOGIFO-X.

### 4.3. DC Disturbance Experiments

To verify the performance of the proposed method further, two DC disturbance experiments were conducted. Figures 16 and 17 show the experimental results under DC offset disturbances of $\Delta u_\alpha = 15\,\text{V}$ and $\Delta i_\alpha = 1\,\text{A}$, respectively, at 1000 r/min.

Figure 16 shows the results when a $\Delta u_\alpha = 15\,\text{V}$ DC offset is applied at 1 s. The flux estimated by SOGIFO fluctuates by 0.003 Wb. This affects its position signal estimation, increasing the position error from 0.623 rad to 0.669 rad, with a speed fluctuation of 23 r/min.

Similar experimental results are shown in Figure 17 for the current disturbance. As shown in Figure 17(a), under a $\Delta i_\alpha = 1\,\text{A}$ DC disturbance applied at 1 s, SOGIFO's estimated flux still shows a 0.003 Wb deviation, leading to a position estimation error of 0.841 rad and speed fluctuation of 17 r/min. However, under TOGIFO-X observations, the rotor flux was accurately estimated, with a speed fluctuation of only 5 r/min.

Based on the analysis of the above experiments, TOGIFO-X possesses a better anti-DC disturbance capability than SOGIFO and can deliver excellent observation performance under practical operating conditions.

### 4.4. Parameter Mismatch Experiment

In actual operation, the parameters of the PMSM vary with changes in internal temperature and skin effect. The stator resistance generally increases as temperature rises. Based on this, two parameter mismatch experiments with $R_s' = 1.5R_s$ were designed in this study.

The experiment involves changing the stator resistance $R_s$ to $1.5R_s$ at 1.2 s. As shown in Figure 18, when the stator resistance varies, the flux linkage deviation estimated by SOGIFO increases from 0.001 Wb to 0.013 Wb. This conse-

quently causes the estimated speed fluctuation and position error to rise to 42 r/min and 0.356 rad, respectively. However, TOGIFO-X can still effectively estimate the flux linkage, with only a slight increase in the estimated speed fluctuation and position error.

## 5. CONCLUSION

This paper proposes the use of TOGIFO-X to overcome the limitations of conventional flux observers in sensorless PMSM control. This algorithm significantly reduces high-order harmonics. It also eliminates the common DC offset issue in existing methods, without changing the fundamental wave's amplitude or phase. Rigorous mathematical derivation, Bode plot analysis, simulation, and physical experiments all verify the reliability of TOGIFO-X in flux estimation. This leads to significant improvements in PMSM operating efficiency and rotor position determination accuracy. Experiments also demonstrated that TOGIFO-X exhibits good dynamic performance and anti-DC disturbance capability, making it a promising candidate for sensorless drives.

## REFERENCES


[1] Chen, S., W. Ding, R. Hu, X. Wu, and S. Shi, "Sensorless control of PMSM drives using reduced order quasi resonant-based ESO and Newton-Raphson method-based PLL," *IEEE Transactions on Power Electronics*, Vol. 38, No. 1, 229–244, 2023.

[2] Wang, G., M. Valla, and J. Solsona, "Position sensorless permanent magnet synchronous machine drives — A review," *IEEE Transactions on Industrial Electronics*, Vol. 67, No. 7, 5830–5842, 2020.

[3] Jiang, Y., W. Xu, C. Mu, J. Zhu, and R. Dian, "An improved third-order generalized integral flux observer for sensorless drive of PMSMs," *IEEE Transactions on Industrial Electronics*, Vol. 66, No. 12, 9149–9160, 2019.

[4] Anayi, F. J. and M. M. A. A. Ibraheemi, "Estimation of rotor position for permanent magnet synchronous motor at standstill using sensorless voltage control scheme," *IEEE/ASME Transactions on Mechatronics*, Vol. 25, No. 3, 1612–1621, 2020.

[5] Zhou, M., S. Cheng, Y. Feng, W. Xu, L. Wang, and W. Cai, "Full-order terminal sliding-mode-based sensorless control of induction motor with gain adaptation," *IEEE Journal of Emerging and Selected Topics in Power Electronics*, Vol. 10, No. 2, 1978–1991, 2022.

[6] Xu, B., L. Zhang, and W. Ji, "Improved non-singular fast terminal sliding mode control with disturbance observer for PMSM drives," *IEEE Transactions on Transportation Electrification*, Vol. 7, No. 4, 2753–2762, 2021.

[7] Dhaouadi, R., N. Mohan, and L. Norum, "Design and implementation of an extended Kalman filter for the state estimation of a permanent magnet synchronous motor," *IEEE Transactions on Power Electronics*, Vol. 6, No. 3, 491–497, 1991.

[8] Zhu, G., A. Kaddouri, L. A. Dessaint, and O. Akhrif, "A nonlinear state observer for the sensorless control of a permanent-magnet AC machine," *IEEE Transactions on Industrial Electronics*, Vol. 48, No. 6, 1098–1108, 2001.

[9] Rahman, M. F., M. E. Haque, L. Tang, and L. Zhong, "Problems associated with the direct torque control of an interior permanent-magnet synchronous motor drive and their remedies," *IEEE Transactions on Industrial Electronics*, Vol. 51, No. 4, 799–809, 2004.

[10] Wu, C., X. Sun, and J. Wang, "A rotor flux observer of permanent magnet synchronous motors with adaptive flux compensation," *IEEE Transactions on Energy Conversion*, Vol. 34, No. 4, 2106–2117, 2019.

[11] Feng, G., C. Lai, K. Mukherjee, and N. C. Kar, "Online PMSM magnet flux-linkage estimation for rotor magnet condition monitoring using measured speed harmonics," *IEEE Transactions on Industry Applications*, Vol. 53, No. 3, 2786–2794, 2017.

[12] Jiang, Y., W. Xu, and C. Mu, "Improved SOIFO-based rotor flux observer for PMSM sensorless control," in *IECON 2017 — 43rd Annual Conference of the IEEE Industrial Electronics Society*, 8219–8224, Beijing, China, 2017.

[13] Zhao, R., Z. Xin, P. C. Loh, and F. Blaabjerg, "A novel flux estimator based on multiple second-order generalized integrators and frequency-locked loop for induction motor drives," *IEEE Transactions on Power Electronics*, Vol. 32, No. 8, 6286–6296, 2017.

[14] Jiang, Y., W. Xu, C. Mu, J. Zhu, and R. Dian, "An improved third-order generalized integral flux observer for sensorless drive of PMSMs," *IEEE Transactions on Industrial Electronics*, Vol. 66, No. 12, 9149–9160, 2019.

[15] Xu, W., Y. Jiang, C. Mu, and F. Blaabjerg, "Improved nonlinear flux observer-based second-order SOIFO for PMSM sensorless control," *IEEE Transactions on Power Electronics*, Vol. 34, No. 1, 565–579, 2019.

[16] Zhang, Y., Z. Yin, F. Gao, and J. Liu, "Research on anti-DC bias and high-order harmonics of a fifth-order flux observer for IPMSM sensorless drive," *IEEE Transactions on Industrial Electronics*, Vol. 69, No. 4, 3393–3406, 2022.